

---

# QCPINN: QUANTUM CLASSICAL PHYSICS-INFORMED NEURAL NETWORKS FOR SOLVING PDES

---

**Afrah Farea**

Computational Science and Engineering Department, Informatics Institute  
Istanbul Technical University  
Istanbul 34469, Turkiye  
farea16@itu.edu.tr@email

**Saiful Khan**

Scientific Computing, Rutherford Appleton Laboratory  
Science and Technology Facilities Council (STFC)  
OX11 0QX, United Kingdom  
saiful.khan@stfc.ac.uk

**Mustafa Serdar Celebi**

Computational Science and Engineering Department, Informatics Institute  
Istanbul Technical University  
Istanbul 34469, Turkiye  
mscelebi@itu.edu.tr

## ABSTRACT

Physics-informed neural networks (PINNs) have emerged as promising methods for solving partial differential equations (PDEs) by embedding physical laws into neural architectures. However, these classical approaches often require large number of parameters for solving complex problems or achieving reasonable accuracy. We investigate whether quantum-enhanced architectures can achieve comparable performance while significantly reducing model complexity. We propose a quantum-classical physics-informed neural network (QCPINN) combining quantum and classical components to solve PDEs with fewer parameters while maintaining comparable accuracy and training convergence. Our approach systematically evaluates two quantum circuit paradigms (e.g., continuous-variable (CV) and discrete-variable (DV)) implementations with four circuit topologies (e.g., alternate, cascade, cross-mesh, and layered), two embedding schemes (e.g., amplitude and angle) on five benchmark PDEs (e.g., Helmholtz, lid-driven cavity, wave, Klein-Gordon, and convection-diffusion equations). Results demonstrate that QCPINNs achieve comparable accuracy to classical PINNs while requiring approximately 10% trainable parameters across different PDEs, and resulting in a further 40% reduction in relative  $L_2$  error for the convection-diffusion equation. DV-based circuits with angle embedding and cascade configurations consistently exhibited enhanced convergence stability across all problem types. Our finding establishes parameter efficiency as a quantifiable quantum advantage in physics-informed machine learning. By significantly reducing model complexity while maintaining solution quality, QCPINNs represent a potential direction for overcoming computational bottlenecks in scientific computing applications where traditional approaches require large parameter spaces.

## 1 Introduction

Recent advancements in machine learning have transformed approaches to solving PDEs, with PINNs emerging as an innovative methodology. PINNs embed physical laws directly into neural network architectures, eliminating the need

for labeled training data while strictly enforcing physical constraints. This approach has demonstrated considerable success in modeling various physical phenomena across scientific and engineering domains. Despite their promise, PINNs face significant limitations when modeling complex physical systems. They often struggle with stiff systems, capturing sharp gradients, and effectively navigating high-dimensional parameter spaces. While increasing model expressivity through additional parameters can address these challenges, this approach introduces new problems: increased computational cost, risk of overfitting, and unstable convergence behavior during training[1]. Such a trade-off between model complexity, generalization, and convergence ability is a fundamental consideration in neural network design.

Quantum computing presents a promising paradigm for overcoming these limitations. With its ability to process high-dimensional data and exploit quantum principles such as superposition and entanglement, quantum algorithms offer unique advantages for solving complex computational problems. For instance, the Harrow-Hassidim-Lloyd (HHL) algorithm has demonstrated theoretical exponential speedups for specific linear systems, while variational quantum algorithms provide practical near-term solutions [2, 3, 4]. Moreover, recent developments [5, 6, 7] indicate that quantum neural networks possess an expressive power that could significantly enhance the learning capabilities for modeling complex physical systems.

Although both PINNs and quantum computing have advanced independently, their integration remains largely unexplored. Several preliminary efforts have emerged: Sedykh et al. proposed HQPINN [8] focus on computational fluid dynamics in 3D Y-shaped mixers; Dehaghani et al. introduced QPINN [9] integrating dynamic quantum circuit with classical computing methodologies for optimal control problems; Trahan et al. [10] investigated both purely quantum and hybrid PINNs, highlighting parameter efficiency but limiting application to parametrized quantum circuit (PQC) networks with simple PDEs. Inspired by Fourier neural operators, Leong et al. recently proposed HQPINN [11]. However, existing research has not comprehensively established whether quantum-enhanced models can improve upon purely classical PINNs across a broad range of PDEs with consistent efficiency and reliability.

We aim to address the limitations of traditional PINNs by integrating quantum computing circuits with classical neural networks. We propose that this hybrid approach can leverage complementary strengths: classical computing’s robustness and quantum computing’s enhanced expressivity and inherent parallelism. Specifically, we believe that such integration will allow us to solve a broad spectrum of PDEs with comparable or improved accuracy and convergence rate, while requiring substantially fewer trainable parameters than classical counterparts.

To this end, we introduce a hybrid architecture named Quantum-Classical Physics-Informed Neural Network (QCPINN). Our approach systematically explores multiple dimensions of the design space: (a) two quantum circuit architectures, e.g., discrete-variable (DV) qubit-based circuits, and continuous-variable (CV) circuits; (b) four circuits topologies, e.g., alternate, cascade, cross-mesh, and layered implementations; and (c) two embedding schemes, e.g., amplitude and angle embedding. We evaluate QCPINN performance across diverse PDEs, including Helmholtz and lid-driven cavity equations, extending our analysis to Klein-Gordon, wave, and convection-diffusion equations. Our comprehensive assessment compares (a) solution accuracy, (b) convergence rates, and (c) parameter efficiency between classical PINNs and our QCPINN variants.

To ensure reproducibility and facilitate broader adoption of our methods, we have made all components of QCPINN open-source code and publicly available on GitHub at <https://github.com/afrah/QCPINN>. This repository serves as both a resource for validating our findings and a foundation for future research in quantum-enhanced physics-informed machine learning, enabling community engagement and collaborative advancement of this emerging field.

## 2 Background

### 2.1 Physics Informed Neural Network (PINNs)

PINNs [12] provide a framework to embed governing physical laws directly into neural network architectures. The PINN loss function combines terms representing governing equations and boundary conditions designed to minimize deviations from physical laws. More formally:

$$\begin{aligned} \mathcal{L}(\theta) &= \arg \min_{\theta} \sum_{k=1}^n \lambda_k \mathcal{L}_k(\theta) \\ &= \arg \min_{\theta} \left( \lambda_1 \mathcal{L}_1(D[u_{\theta}(\mathbf{x}); \mathbf{a}] - f(\mathbf{x})) + \sum_{k=2}^n \lambda_k \mathcal{L}_k(B[u_{\theta}(\mathbf{x})] - g_k(\mathbf{x})) \right), \end{aligned} \tag{1}$$

where,  $n$  denotes the total number of loss terms,  $\lambda_k$  are the weighting coefficients, and  $\theta$  represents trainable parameters. Here,  $[D[u_\theta(\mathbf{x}); \mathbf{a}]$  and  $[B[u_\theta(\mathbf{x})]$  are the arbitrary differential operators and initial/boundary conditions, respectively, that are applied to the output of the neural network  $u_\theta(\mathbf{x})$ . While the initial and boundary conditions ensure that the network output satisfies predefined constraints at specific spatial or temporal locations, the physics loss acts as a regularizer, guiding the network to learn physically consistent solutions and preventing overfitting to sparse or noisy data. The balance between these loss components is crucial for achieving accurate solutions, as improper weighting can lead to underfitting the initial/boundary conditions or failing to capture the system dynamics correctly.

## 2.2 Continuous Variable (CV) QNN

In photonic quantum computing, CV computation addresses quantum states with continuous degrees of freedom, such as the position ( $x$ ) and momentum ( $p$ ) quadratures of the electromagnetic field. The computational space is, in principle, unbounded, involving infinite-dimensional Hilbert spaces with continuous spectra. To make these simulations computationally feasible, a cutoff dimension is employed to limit the number of basis states used for approximation. The computational state space is defined as  $r = n^m$ , where  $m$  represents the number of qumodes and  $n$  is the cutoff dimension. For example, with three qumodes and a cutoff dimension of 2, the state space is 8-dimensional. Ideally, higher cutoff dimensions (up to a certain threshold) yield more precise results but at the cost of increased computational complexity.

In this work, we adhere to the affine transformation proposed in [13], embedding the quantum circuit into the PINN framework to solve PDEs. The proposed circuit ansatz comprises a sequence of operations that manipulate quantum states in phase space. Each layer of the CV-based QNN consists of the following key components:

1. **Interferometers** ( $U_1(\theta_1, \phi_1)$  and  $U_2(\theta_2, \phi_2)$ ): Linear optical interferometers perform orthogonal transformations, represented by symplectic matrices. These transformations adjust the state by applying rotation and mixing between modes, corresponding to beam splitting and phase-shifting operations.
2. **Squeezing Gates** ( $S(r, \phi_s)$ ): These gates scale the position and momentum quadratures independently, introducing anisotropic adjustments to the phase space. The ability to encode sharp gradients using squeezing gates is particularly appealing for PDE solvers, as it allows fine-tuning of local characteristics [8].
3. **Displacement Gates** ( $D(\alpha, \phi_d)$ ): These gates shift the state in phase space by adding a displacement vector  $\alpha$ , effectively translating the state globally without altering its internal symplectic structure.
4. **Non-Gaussian Gate** ( $\Phi(\lambda)$ ): To introduce nonlinearity, a non-Gaussian operation, such as a cubic phase and Kerr gates, is applied. This step enables the neural network to approximate nonlinear functions and enhances the ability to solve complex, nontrivial PDEs.

These components together mimic the classical affine transformation such that:

$$L(|x\rangle) = |\Phi(Mx + b)\rangle = \Phi(D \circ U_2 \circ S \circ U_1), \quad (2)$$

where  $M$  represents the combined symplectic matrix of the interferometers and squeezing gates,  $x$  is the input vector in the phase space,  $b$  is the displacement vector, and  $\Phi$  is the nonlinear transformation.

While such a model exhibits intriguing theoretical properties, their practical implementation in real-world problem-solving seems to suffer from fundamental stability issues. This is mainly due to their inherent sensitivity and reliance on continuous degrees of freedom, which complicate optimization compared to DV-based approaches. This sensitivity stems from several factors, including the precision required for state preparation, noise from decoherence, and the accumulation of errors in variational quantum circuits. Furthermore, the transformations involved in CV quantum circuits are prone to numerical instabilities, particularly when optimized using gradient-based methods, as seen in the following section. Although foundational studies about the barren plateau problem, such [14, 15, 16], primarily address DV circuits systems, the analysis indicates that similar issues can arise in CV quantum systems. In particular, the infinite-dimensional Hilbert space and the continuous nature of parameterization can exacerbate barren plateau effects.

## 2.3 Discrete Variable (DV) QNN

While CV-circuit quantum models do not inherently provide affine transformations as a core feature like CV-based QNNs, they can achieve affine-like behaviour through parameterized single-qubit rotations, controlled operations, and phase shifts for amplitude adjustments. Therefore, the affine transform of equation (2) can be reinterpreted to align with their architecture such that:

1.  $\mathbf{Mx} + \mathbf{b}$ : can be achieved through a combination of parameterized quantum gates:
  - $U_1, U_2$ : A unitary operator that can be represented by parameterized single-qubit rotations, such as  $R_x(\theta), R_y(\theta)$ , or  $R_z(\theta)$ .
  - $S$ : A sequence of controlled gates (e.g., CNOT, CZ) responsible for introducing entanglement, which enables the representation of correlated variables and interactions.
  - $D$ : Data encoding circuits that map classical data into quantum states through techniques such as basis embedding, amplitude embedding, or angle embedding.
2. **Non-linear Activation ( $\Phi$ )**: DV-circuit QNNs lack intrinsic quantum nonlinearity due to the linearity of quantum mechanics. However, classical measurements with/without non-linear activation, like *Tanh* and *ReLU*, can be applied to the output between quantum layers [17, 18].

### 3 Related Work

In the domain of PDE solvers, quantum algorithms can be broadly categorized into two primary approaches: (a) exclusively quantum algorithms and (b) hybrid quantum-classical methods.

#### 3.1 Exclusively Quantum Algorithms

Exclusively quantum algorithms for solving PDEs typically leverage unitary operations and quantum state embedding techniques to achieve computational advantages. In contrast to neural networks, exclusively quantum algorithms use fixed quantum circuit structures with no trainable parameters. The celebrated Harrow-Hassidim-Lloyd (HHL) algorithm is an example of this category, which provides exponential speedups for solving linear systems under specific conditions [19]. Extensions of the HHL algorithm have been applied to solve sparse linear systems derived from discretized linear [20, 21] or nonlinear [22] PDEs, leveraging numerical techniques such as linear multistep method [23], Chebyshev pseudospectral method [24], and Taylor series approximations [25]. In fluid dynamics applications, lattice-gas quantum models have been examined for directly solving PDEs [26, 27] or PDEs derived from ODEs through methods such as the Quantum Amplitude Estimation Algorithm (QAEA) [28, 29].

Despite these advancements, purely quantum algorithms for solving PDEs encounter practical challenges such as requirements for quantum error correction [30, 31, 32], limitations in circuit depth [33, 27, 34], and bottlenecks in data embedding [35, 36, 37]. These obstacles, among others, limit the near-term viability of exclusively quantum PDE solvers on today’s noisy intermediate-scale quantum (NISQ) devices.

#### 3.2 Hybrid Quantum-Classical Approaches

Hybrid quantum-classical approaches have emerged as promising solutions to overcome the limitations of exclusively quantum algorithms. These methods combine the robustness, maturity, and stability of classical computation with the enhanced capacity, expressivity, and inherent parallelism of quantum systems. While classical components can efficiently handle pre-/post-processing, optimization, and error stabilization; quantum layers can capture intricate patterns, solve sub-problems, and accelerate specialized computations.

Within this hybrid paradigm, Quantum Neural Networks (QNNs) have demonstrated universal approximation capabilities for continuous functions when implemented with sufficient depth, width, and well-designed quantum feature maps [38, 39, 40]. For instance, Salinas et al.[41] showed that single-qubit networks with iterative input reuploading can approximate bounded complex functions, while Goto et al.[42] established universal approximation theorems for quantum feedforward networks. Moreover, Schuld et al.[5] revealed that the outputs of parameterized quantum circuits (with suitable data embedding and circuit depth) can be expressed as truncated Fourier series, thereby providing theoretical support for the universal approximation ability of QNNs. Furthermore, Liu et al.[43] provided formal evidence of quantum advantage in function approximation. These developments not only support applications in solving PDEs and optimization tasks but also extend to other computational tasks such as quantum chemistry [44], materials science [45, 46], and pattern recognition [47] to name a few.

A well-known example of this integrated approach is the Variational Quantum Algorithms (VQA), also known as Variational Quantum Circuits (VQC). These algorithms employ parameterized quantum circuits with tunable gates optimized through classical feedback loops. VQA implementations for solving PDEs include the Variational Quantum Eigensolver (VQE)[48, 49], Variational Quantum Linear Solver (VQLS)[50], and Quantum Approximate Optimization Algorithm (QAOA)[51], as well as emerging methods like Differentiable Quantum Circuits (DQCs)[52, 53], quantum kernel methods [54], and Quantum Nonlinear Processing Algorithms (QNPA) [55].

The aforementioned methods primarily utilize qubit-based quantum computing, which represents the predominant paradigm in quantum computing literature. However, continuous-variable quantum computing (CVQC) [56] offers an alternative computational model that leverages continuous degrees of freedom, such as quadratures and electromagnetic field momentum as discussed in section 2.2. For instance, in [57], Gaussian and non-Gaussian gates were used to manage continuous degrees of freedom, offering enhanced scalability and expressivity for continuous systems. For consistency, we refer to qubit-based models as discrete-variable (DV) circuit models throughout this paper.

Recently, VQA methods have been extended to Physics-informed quantum neural networks (PIQNN) [58, 9, 10, 8, 11], broadening their applicability across physics and engineering domains. These hybrid methods offer several distinct advantages when implemented within the PINN framework.

Firstly, these models enable the flexible configuration of inputs and outputs independent of qubit/qumode counts or quantum layer depth, making them particularly effective for scenarios where the input dimension (e.g., temporal and spatial coordinates) differs from output dimensions (e.g., dependent variables like velocity, pressure, and force).

Secondly, hybrid approaches facilitate increased trainable parameter counts without necessitating deeper quantum circuits, additional qubits, or higher cutoff dimensions in CV quantum systems. These factors are particularly crucial in the NISQ era, where hardware constraints impose strict limits on circuit depth and coherence times, making deeper quantum networks computationally expensive and impractical [59, 60].

Thirdly, these qualities are especially advantageous for PINNs, where shallow network architectures are favored to optimize the balance between computational efficiency and solution accuracy [61, 62, 63, 64]

Finally, a substantial benefit of such hybrid models is the integration of automatic differentiation within both classical and quantum networks. This capability, supported by contemporary software packages like PennyLane [65] and TensorFlow Quantum [66], enables the automatic computation of derivatives as variables are directly incorporated into the computational graph. This approach simplifies PINN implementation and facilitates the efficient handling of complex physics-informed loss functions and higher-order derivatives.

The work presented here is related to the approaches in [8, 9, 10, 11], but with several key differences. While HQPINN [8] focuses specifically on computational fluid dynamics in 3D Y-shaped mixers using a fixed quantum depth with an infused layer structure, the QPINN [9] integrates a dynamic quantum circuit combining Gaussian and non-Gaussian gates with classical computing methodologies within a PINN framework to solve optimal control problems. In addition, the model proposed in [10] investigates both purely quantum and hybrid PINNs, highlighting parameter efficiency but relying on limited PQC networks and addressing primarily simple PDEs. Recently proposed HQPINN [11], inspired by Fourier neural operator (FNO) [67], introduces a parallel hybrid architecture to separately model harmonic and non-harmonic features before combining them for output.

## 4 Quantum-Classical Physics-Informed Neural Networks (QCPINN)

Figure 1 illustrates a high-level overview of our proposed QCPINN. The preprocessor consists of a two-layer neural network architecture, ensuring that the overall framework is sufficiently shallow for efficient training while also being deep enough to capture essential transformations. Each layer is composed of 50 neurons. The first layer of the preprocessor performs a linear transformation to modify the input dimension, followed by a  $Tanh$  activation function to introduce non-linearity. The second layer subsequently maps the transformed inputs to the QNN layer (or classical NN layer). Likewise, the postprocessor layer replicates the preprocessor structure with appropriate dimensions, ensuring a symmetric transformation between classical and quantum representations. This design offers flexibility in managing quantum feature representations while ensuring the higher-order differentiability required for residual loss in PINNs.

In the QNN layer of figure 1, we implemented two quantum models: (a) the continuous-variable or CV-circuit, which is a hybrid model that leverages a photonic-based quantum neural network; and (b) the discrete-variable or DV-circuit, which uses qubit-based quantum circuits. We also implemented classical models in the NN layer of figure 1, which provides us with classical PINN models to compare their performance with our quantum models.

### 4.1 CV-circuit QCPINN

The CV-circuit QCPINN consists of three primary components: a preprocessor network, a CV-circuit quantum network (the QNN layer of figure 1), and a postprocessor network. The quantum network implementation follows the framework introduced in [13] and is outlined in algorithm 1. This network comprises multiple quantum layers, each executing a sequence of quantum operations. By structuring the network this way, the complete circuit depth scales to  $(2n + 3)L$ , and the number of trainable quantum parameters grows to  $\mathcal{O}(n^2L)$ , where  $n$  is the number of qumodes and  $L$  is the number of layers.

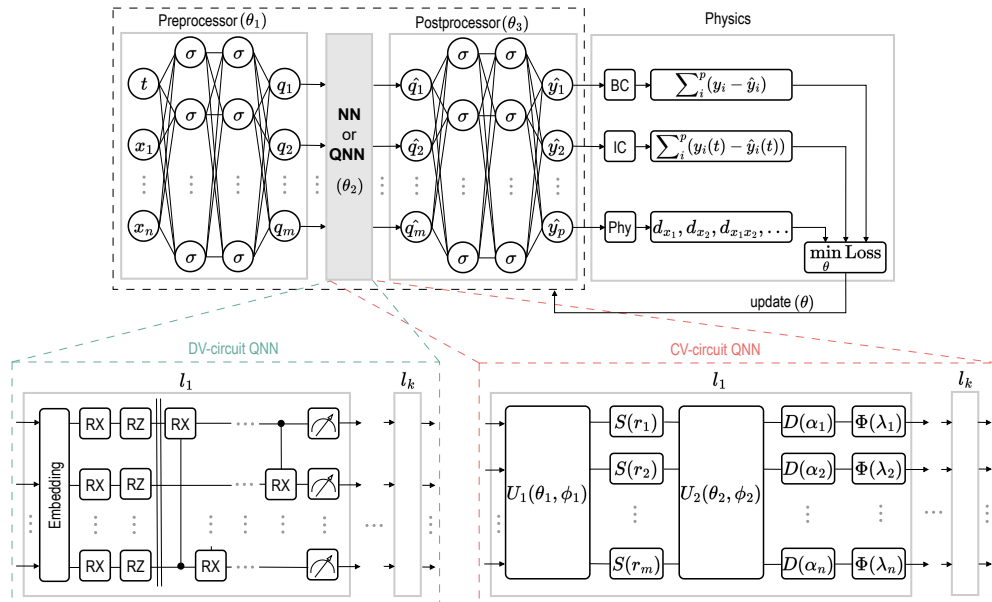


Figure 1: Architecture of the quantum-classical physics-informed neural network (QCPINN) framework. The figure illustrates the hybrid structure: a classical preprocessor encodes the inputs, which are then fed into the QNN or classical neural network (NN). The QNN is implemented as either CV-circuit or DV-circuit with  $k$  layers. A classical postprocessor then decodes the QNN or NN outputs. The integrated loss function concurrently minimizes PDE residuals and initial/boundary condition errors, ensuring the model adheres to physical constraints throughout training.

Table 1: Various circuit ansätze used to examine the circuits in figure 2 where  $n$  is the number of qubits, and  $L$  is the number of layers.

Topology	Circuit Depth	Circuit Connectivity	Number of Parameters	Number of two-qubit gates
alternate	$6L$	Nearest-neighbor	$4(n-1)L$	$(n-1)L$
cascade	$(n+2)L$	Ring topology	$3nL$	$nL$
cross-mesh	$(n^2 - n + 4)L$	All-to-all	$(n^2 + 3n)L$	$(n^2 - n)L$
layered	$6L$	Nearest-neighbor	$4(n-1)L$	$(n-1)L$

## 4.2 DV-circuit QCPINN

The DV-circuit QCPINN consists of three primary components: a preprocessor network, a DV-circuit quantum network (the QNN layer of figure 1), and a classical postprocessor network. The quantum network employs a custom DV Quantum Network, which executes quantum operations on the preprocessed data. Figure 2 illustrates four proposed PQC ansätze named after their topology: layered, cross-mesh, cascade, and alternate. These circuits are inspired from [68, 69, 70, 58]. Table 1 presents various parameterized quantum circuit topologies across the key descriptors, circuit depth, connectivity, number of parameters, and the number of two-qubit gates.

According to equation (10) in [71], a hardware-efficient ansatz (HEA) is defined as:

$$U(\theta) = \prod_k U_k(\theta_k) W_k, \quad (3)$$

where, each layer  $k$  alternates between single-qubit parameterized rotations,  $U_k(\theta_k)$ , and an entangling operation,  $W_k$ . All four circuits in figure 2 adhere to this HEA structure. The selected circuit ansätze also agree with the affine transformation discussed in section 2.

The cross-mesh ansatz implements an all-to-all connectivity scheme, facilitating extensive interaction between qubits, which enhances its ability to explore the Hilbert space. The circuit depth scales as  $\mathcal{O}(n^2 - n + 4)L$ , while the number of trainable parameters is  $(n^2 + 3n)L$ . The use of global entanglement fosters strong correlations between qubits; however, it results in greater circuit depth, resource demands, and training difficulties [16]. This circuit's total number of two-qubit gates is also significantly higher than in other ansätze (refer to table 1).

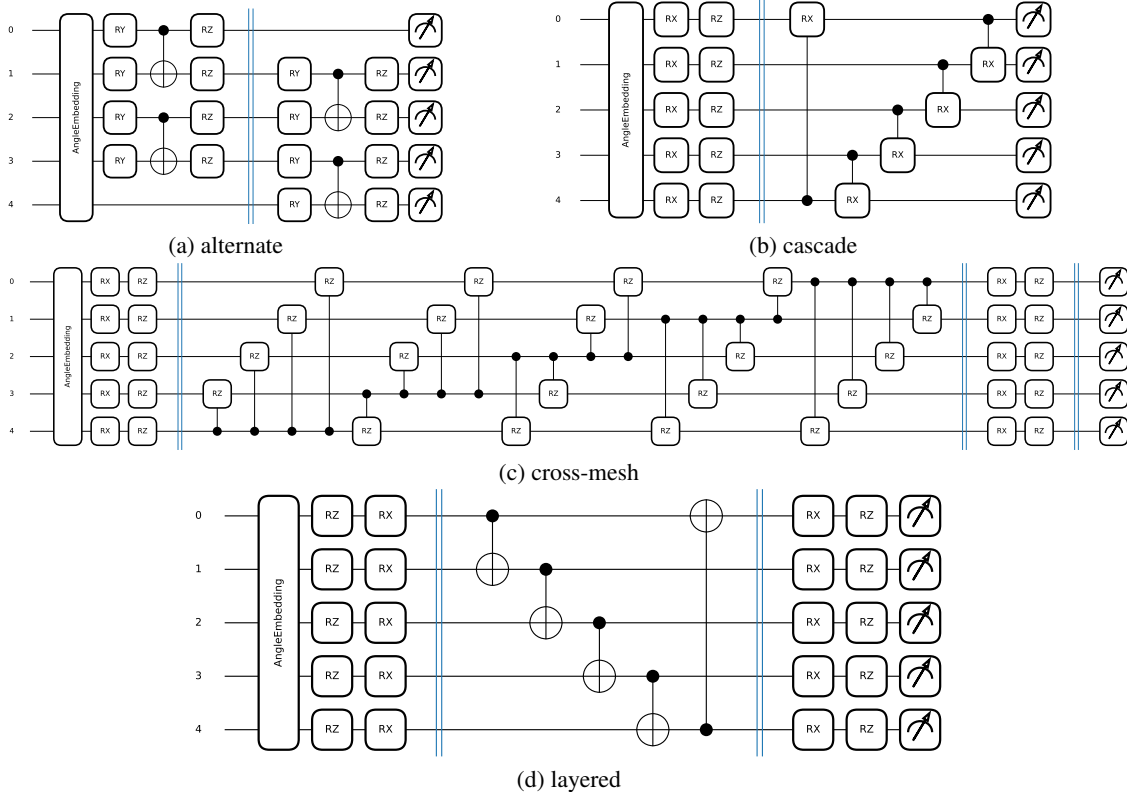


Figure 2: PQC circuits are illustrated with five qubits and angle embedding as an example, and they are also compared with amplitude embedding. The square-shaped boxes represent parameterized rotation gates. The detailed characteristics of these circuits are in table 1.

The cascade ansatz balances expressivity and hardware efficiency by employing a ring topology for qubit connectivity. This design facilitates efficient entanglement while keeping the circuit depth manageable at  $(n + 2)L$ . The circuit contains  $3nL$  trainable parameters, making it more efficient than cross-mesh while maintaining reasonable expressivity. Incorporating controlled rotation gates ( $CR_X$ ) improves entanglement compared to CNOT gates and increases the circuit’s capacity to explore the Hilbert space. Furthermore, the requirement for two-qubit gates is fewer than that of cross-mesh, thus lowering the overall computational cost.

The layered ansatz features a structured design that includes alternating rotation and entangling layers. Each qubit undergoes parameterized single-qubit rotations, typically utilizing  $R_X$  and  $R_Z$  gates. Entanglement is achieved through nearest-neighbor CNOT gates, ensuring compatibility with hardware constraints while maintaining efficient connectivity. Compared to the cross-mesh’s all-to-all connectivity or the cascade’s ring topology, the layered architecture represents a compromise between expressivity and hardware efficiency.

The alternate ansatz uses an alternating-layer structure featuring nearest-neighbor CNOT gates, ensuring effective entanglement while maintaining a manageable circuit depth of  $6L$ . The total number of trainable parameters in this circuit  $4(n - 1)L$  aligns with the layered ansatz. The entanglement structure determined by the alternating CNOT layers, offers the highest level of entangling capability among the circuits studied. Consequently, the cross-mesh ansatz provides the largest parameter count and highest expressivity, whereas the alternate circuit excels in entangling capabilities.

Compared to the QNN models discussed above, we can see that the classical feedforward neural networks (NNs) exhibit a more flexible scaling pattern, with parameters  $\mathcal{O}(h^2L)$ , where  $h$  denotes the number of hidden neurons (assuming a fixed width  $h$  in all hidden layers) with independent selection of  $h$ . Therefore, while classical models depend on deep architectures and larger parameter counts, quantum networks achieve expressivity by utilizing intrinsic quantum correlations and exponential scaling of the Hilbert space.

## 5 Implementation and Training Details

We used PyTorch’s automatic differentiation to compute the gradients for both classical and quantum parameters. The training was carried out with a batch size of 64 and a maximum of 20,000 epochs in all case studies except in the cavity problem, where we used 12,500 maximum iterations. The Adam optimizer was used to ensure stable convergence. These settings were uniformly applied across all study cases to provide a consistent basis for comparison. Additionally, training data was selected through the Sobol sequence for the cavity problem and random sampling for all other cases.

While other training configurations, such as increasing the number of iterations or adjusting the batch size, could yield better performance, the goal is to evaluate the models under identical conditions. Given the near-infinite hyperparameter space, this controlled evaluation ensures a fair assessment of the relative strengths and limitations of each approach. It is also important to acknowledge that the quantum experiments conducted in this study were performed using simulations rather than actual quantum hardware. These simulations inherently operate at significantly reduced speeds compared to their classical counterparts due to the substantial computational overhead associated with emulating quantum circuits on classical machines. Future implementations on actual quantum hardware would eliminate this simulation overhead, potentially revealing additional performance characteristics not captured in the current study.

In our initial implementation, we realized that the experiments on the CPU were faster than those on the GPU. This is likely due to our study’s relatively small batch size, circuit complexity, and limited number of qubits/qumodes: five qubits for DV-circuit models and two qumodes for CV-based models. Moreover, the quantum backends employed in our experiments are not optimized for GPU efficiency. Considering these limitations, we have chosen to conduct our experiments on a CPU system with 6148 CPUs (each operating at 2.40 GHz) and 192 GB of RAM. Further details on training configurations and implementation strategies are provided in the following subsections.

### 5.1 CV-circuit QCPINN

We used the PennyLane framework [65] with the Strawberry Fields Fock backend [72] to develop and train our CV-circuit QCPINN model. Each CV-circuit layer was configured for two qumodes with a cutoff dimension of 20. Quantum parameters were initialized using controlled random distributions, with small values for active parameters (e.g.,  $r_{\text{squeeze}}$ ,  $r_{\text{disp}}$ ) to ensure numerical stability. Classical PINN’s layers were initialized using Xavier initialization. During training, position quadrature (X) expectation measurements are performed on each qumode to extract continuous-valued features from the quantum state. These measurements, implemented using the QuadOperator with  $\phi=0.0$ , capture the position-space representation of the quantum information and provide the output to the following classical post-processing layers.

CV-circuit operations are carefully managed to ensure numerical stability. For instance, squeezing operations are highly sensitive to large values, as excessive squeezing amplifies quadrature fluctuations, which increases photon number variance and truncation errors in Fock-space representations [73]. Similarly, displacement operations are constrained to prevent quantum states from exceeding computational cutoffs, as this can introduce simulation errors [74]. Likewise, Kerr interactions cause phase shifts that scale quadratically with photon numbers, making them highly sensitive to large values [75].

Therefore, we used a learning rate of  $1.0 \times 10^{-4}$  to address the model’s sensitivity to gradient updates. A ReduceLROnPlateau scheduler was implemented with a patience of 20 epochs, decreasing the learning rate by a factor of 0.5 when no improvement was observed, down to a minimum of  $1.0 \times 10^{-6}$ . Additionally, we applied gradient clipping to prevent exploding gradients, restricting their norm to a maximum of 0.1.

We scaled the training parameters by small factors to further stabilize the CV transformations. While this can alleviate the instability and prevent divergence in quantum state evolution, it can also introduce the vanishing gradient problem. This issue is well-documented in classical neural network literature and occurs when excessively small initialization values diminish gradients during backpropagation, slowing or even halting the learning process.

### 5.2 DV-circuit QCPINN

We used Adam optimizer with a learning rate of 0.005 to train the DV-circuit QCPINN. A learning rate scheduler, ReduceLROnPlateau, is employed to adjust the learning rate when the loss plateaus dynamically. Specifically, the scheduler reduces the learning rate by a factor of 0.9 if no improvement is observed for 1000 consecutive epochs, promoting stability and convergence. Furthermore, the training function applies gradient clipping to prevent exploding gradients, clipping them according to their norm to ensure they do not exceed a unity value. During training, Pauli-Z expectation measurements are performed on each qubit to extract features from the quantum state.



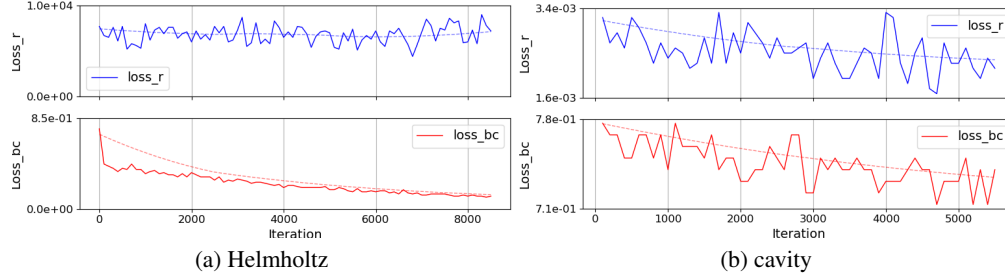


Figure 3: The training convergence behavior of the CV-circuit QCPINN model when solving (a) Helmholtz and (b) lid-driven cavity. The terms “loss\_r” and “loss\_bc” refer to residual and boundary losses. The “loss\_bc” shows a decreasing trend, indicating improvements in satisfying the boundary conditions; however, the overall decrease is below expectation. The “loss\_r” exhibits significant fluctuations and does not display a noticeable reduction, suggesting difficulties in minimizing the residual error of the governing equation.

### 5.3 Classical PINN Model

The classical baseline model consists of three main components: a preprocessing network, a neural network NN, and a postprocessing network (as shown in figure 1). The NN differs between two configurations: (a) In model-1, it includes two fully connected layers, each containing 50 neurons with a Tanh activation function between layers, and (b) In model-2, the NN is entirely omitted, meaning only the preprocessing network and the postprocessing network are kept, simplifying the model’s structure.

These two models represent different levels of complexity, with model-1 having more layers and, consequently, a higher number of trainable parameters compared to model-2. We use these classical models to evaluate and compare the performance of the proposed hybrid models in figure 1. Training settings, including the optimizer and batch size, were kept consistent with the QCPINN models to allow for a fair comparison between classical and quantum-enhanced approaches. The learning rate is 0.005

### 5.4 PDEs

We implemented five distinct PDEs, which include the Helmholtz, the time-dependent 2D lid-driven cavity, the 1D wave, the Klein-Gordon, and a convection-diffusion problems. The mathematical formulation, boundary conditions, and corresponding loss function designs for each PDE are detailed in B.

## 6 Results

At the outset of our project, we implemented the CV and DV-circuits for QCPINN and began testing with two complex benchmark problems: Helmholtz and lid-driven cavity. The CV-circuit exhibited instabilities, and the following subsection provides an overview of our findings and efforts to enhance the results of the CV-circuit. In contrast, the DV-circuit showed promising results; for that reason, we present the results of the DV-circuits in the subsequent subsections in detail.

### 6.1 CV-circuit QCPINN

The CV-circuit implementation of the QCPINN shows substantial sensitivity to large values, as we can see the residual loss of both the Helmholtz and lid-driven cavity equations in figure 3, likely due to the nature of the parameterized CV quantum layers. Specifically, the small scaling factors applied to the trainable parameters of the CV-circuit (related to squeezing, displacement, and Kerr operations; refer to algorithm 1) limit the training capability of the quantum layers. This restricts their capacity to capture complex solution dynamics. As a result, the network prioritizes satisfying the boundary conditions while struggling to minimize the residual loss, which involves higher-order derivatives.

We investigated various normalization techniques to enhance the training stability of the model. However, these often resulted in information loss without any notable improvement in training stability. For example, we applied the Chebyshev feature mapping [29, 52] to normalize the inputs, and we also experimented with random neural networks paired with Gaussian smoothing [76]. Unfortunately, neither of these adjustments proved effective.

Table 2: Comparison of the performance of our DV-circuit QCPINN models against classical PINN approaches in solving the Helmholtz equation. We evaluate eight quantum configurations (combining two embedding methods with four different circuit topologies) alongside two classical neural network models. The comparison metrics include the number of trainable parameters required by each model, the relative  $L_2$  error in % (measuring solution accuracy), and the final training loss value achieved.  $u$  and  $f$  are the PDE solution and the force term.

	Embedding	Topology	# Parameters	Relative $L_2$ Error (%)	Final Loss
DV-circuit	amplitude	alternate	781	$u$	$2.14e + 01$
				$f$	$1.21e + 01$
		cascade	771	$u$	$1.99e + 01$
				$f$	$4.97e + 00$
	cross-mesh	836	$u$	$1.77e + 01$	
			$f$	$3.76e + 00$	
	layered	781	$u$	$4.05e + 01$	
			$f$	$7.54e + 00$	
angle	alternate	781	$u$	$9.15e + 00$	
			$f$	$4.15e + 00$	
	cascade	771	$u$	$4.12e + 00$	
			$f$	$1.64e + 00$	
cross-mesh	836	$u$	$1.18e + 01$		
		$f$	$3.76e + 00$		
layered	781	$u$	$2.35e + 01$		
		$f$	$5.73e + 00$		
classical PINN	model-1		7851	$u$	$3.18e + 01$
				$f$	$6.40e + 00$
	model-2		2751	$u$	$6.72e + 00$
				$f$	$2.83e + 00$

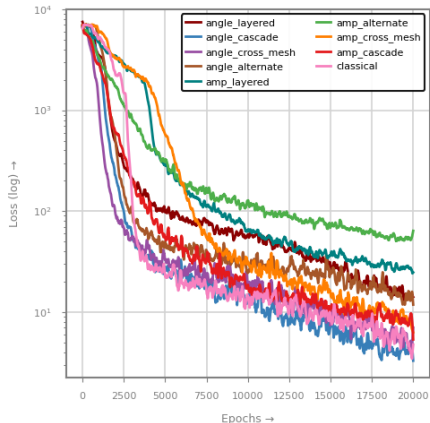


Figure 4: Comparison of the training convergence history of our DV-based QCPINN models compared to classical PINN when solving the Helmholtz equation. The plots track the performance over 20,000 epochs, showing how QCPINN performs with two different embedding methods across four circuit topologies. For comparison, we include the classical neural network model-2, which outperforms model-1 in our experiments.

Therefore, we explored various parameter initializations to mitigate the gradient decay (discussed in section 5.1). This attempt was ineffective, and we believe that alternative optimization strategies beyond gradient descent may be beneficial in addressing this issue, which is beyond the scope of this work.

## 6.2 DV-circuit QCPINN

The DV-circuit QCPINNs show stable performance compared to the CV-circuit QCPINNs. Therefore, in the remainder of this paper, we discuss the results of the DV-circuit QCPINN in detail. Initially, we will focus on solving two PDE equations using DV-circuits: Helmholtz and cavity. Next, we will test the models to validate their generalizability on three additional equations: wave, Klein-Gordon, and convection-diffusion. The performance of the DV-circuit, with variations in two embeddings and four topologies, is compared against that of two classical models.

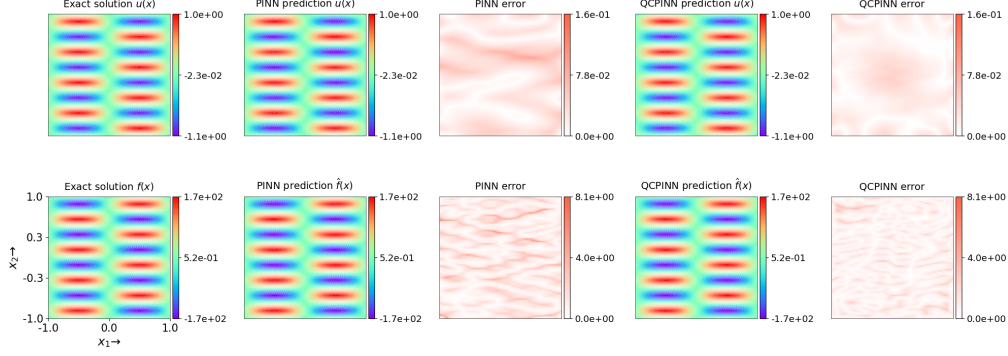


Figure 5: Comparison of the exact solution and the model predictions for the Helmholtz equation: the classical PINN model-2 (which outperforms model-1), and our DV-circuit QCPINN using angle embedding (which outperforms amplitude embedding) with cascade topology (which outperforms the other three topologies). The first row shows the PDE solution  $u$ , while the second row shows the force field ( $f$ ).

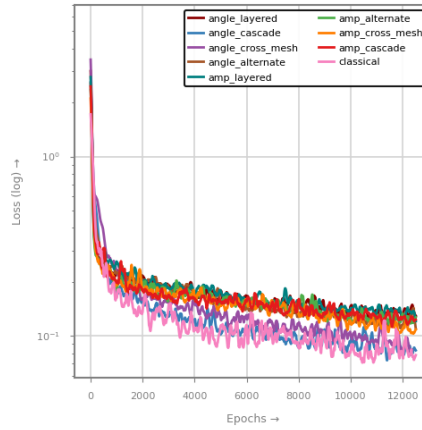


Figure 6: Comparison of the training convergence history of our DV-based QCPINN models compared to classical PINN when solving the lid-driven cavity equation. The plots track the performance over 12500 epochs, showing how QCPINN performs with two different embedding methods across four circuit topologies. For comparison, we include the classical neural network model-2, which outperforms model-1 in our experiments.

### 6.3 Helmholtz Equation

Table 2 presents the performance of the DV-circuit QCPINN models in solving the Helmholtz equation 4 and comparing the results with classical models. The results show that the cascade topology consistently outperforms other topologies, achieving the lowest final training loss and low relative  $L_2$  testing errors. In contrast, the layered and alternate circuit topologies show higher final training losses, especially for the layered model in amplitude embedding.

Figure 4 compares the training loss convergence of DV-circuit QCPINN models to the classical PINN when solving the Helmholtz equation. The results indicate that DV-based quantum models display controlled convergence with relatively stable training dynamics. Moreover, among the various embedding schemes and circuit topologies, the angle-encoded cascade circuit demonstrates the most competitive performance, achieving a loss level close to the best classical model while utilizing approximately 72% fewer parameters

Figure 5 visualizes the exact and predicted solutions for the Helmholtz equation. It also shows the prediction errors of both the best classical model and the angle-cascade QCPINN. While the classical model captures the overall structure, it exhibits noticeable discrepancies, as shown in the absolute error maps, which reveal significant deviations near the boundaries and at regions of sharp local gradients. In contrast, the predictions from the angle-cascade QCPINN model closely align with the exact solutions while using fewer parameters than the classical approach.

Table 3: Comparison of the performance of our DV-circuit QCPINN models against classical PINN approaches in solving the lid-driven cavity equation. We evaluate eight quantum configurations (combining two embedding methods with four different circuit topologies) alongside two classical PINNs. The comparison metrics include the number of trainable parameters required by each model, the relative  $L_2$  error in %, and the final training loss value achieved.  $u$ ,  $v$ , and  $p$  are the velocity components and the pressure values, respectively.

	Embedding	Topology	# Parameters	Relative $L_2$ Error (%)	Final Loss	
DV	amplitude	alternate	933	$u$	$6.441e + 01$	
				$v$	$8.439e + 01$	
				$p$	$6.102e + 01$	
		cascade	928	$u$	$6.670e + 01$	
				$v$	$8.409e + 01$	
				$p$	$6.365e + 01$	
	cross-mesh	988	$u$	$7.073e + 01$		
			$v$	$4.893e + 01$		
	angle	alternate	933	$u$	$4.041e + 01$	
				$v$	$4.683e + 01$	
				$p$	$4.746e + 01$	
		cascade	928	$u$	$2.745e + 01$	
$v$				$2.081e + 01$		
$p$				$4.791e + 01$		
cross-mesh	988	$u$	$2.035e + 01$			
		$v$	$2.071e + 01$			
classical PINN	model-1	8003	$u$	$2.103e + 01$		
			$v$	$3.027e + 01$		
			$p$	$2.317e + 01$		
			model-2	2903	$u$	$3.830e + 01$
					$v$	$2.924e + 01$
					$p$	$4.106e + 01$

## 6.4 Time-dependent 2D Lid-driven Cavity Equation

Table 3 presents the performance of the QCPINN methods for solving the lid-driven cavity equation 5. Among the DV-circuit QCPINN models, cascade achieves the best overall performance, demonstrating good convergence properties with the lowest final training loss. Model using angle embedding and cross-mesh topology also performs well, achieving the lowest final training loss and highlighting its effectiveness in this setting. Specifically, the angle-cascade quantum model achieves comparable performance to the best classical model while requiring only 12% of the parameters.

Figure 6 compares the training loss convergence of various DV-circuit QCPINN models with a classical PINN while solving the lid-driven cavity equation. The loss curves indicate that all DV-based models achieve stable convergence with minimal oscillations. Similar to figure 6, the angle embedding with the cascade topology circuit in figure 4 closely matches the loss level of the best classical model.

Figure 7 visualizes the results obtained using the finite element method (FEM) alongside the predicted solutions for the lid-driven cavity equation 5. It also shows the prediction errors for both the best classical model and the angle-cascade QCPINN. The classical PINN model and the angle-cascade QCPINN effectively capture the main flow features. The absolute error distributions (third and fifth rows) reveal distinct patterns in both velocity components and pressure fields. Both models exhibit higher errors near the top moving lid for velocity components, where the flow experiences the most significant shear.

## 6.5 Generalizing Our Solution

Our experiments with the Helmholtz and lid-driven cavity problems, outlined in sections 6.3 and 6.4, revealed that the angle-cascade variant of the DV-circuit QCPINN architecture consistently outperforms other configurations. To validate the robustness of the angle-cascade QCPINN architecture across diverse physical systems, we expanded our evaluation to three additional canonical PDEs: the wave equation 6, the Klein-Gordon equation 7, and the convection-diffusion

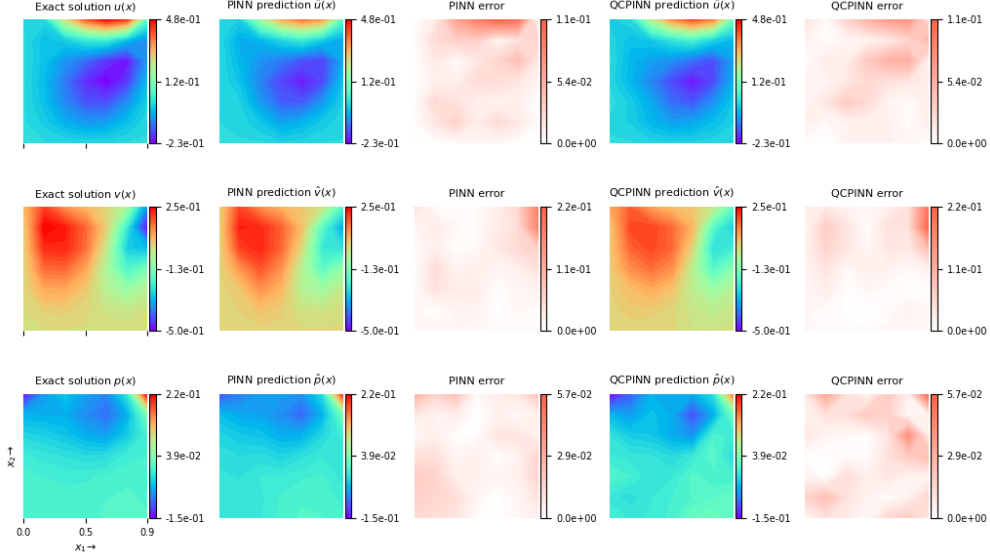


Figure 7: Comparison of the reference FEM solution and the model predictions for the lid-driven cavity equation: the classical PINN model-2 (which outperforms model-1), and our DV-circuit QCPINN using angle embedding (which outperforms amplitude embedding) with cascade topology (which outperforms the other three topologies). The first and second rows show the velocity field ( $u$  and  $v$ ), while the third row shows the pressure field ( $p$ ).

Table 4: Comparison of our DV-circuit QCPINN using angle embedding (which outperforms amplitude embedding) with cascade topology (which outperforms the other three topologies) with the two classical PINN models for solving wave, Klein-Gordon, and convection-diffusion equations. The comparison metrics include the number of trainable parameters required by each model, the relative  $L_2$  error in %, and the final training loss value achieved.  $u$  and  $f$  are the exact solutions and the source term, respectively.

PDEs	Method	# Parameters	Relative $L_2$ Error (%)	Final Loss	
wave Eq. 6	angle-Cascade	771	$u$ 1.02e + 01	0.083	
	classical PINN	model-1	7851	$u$ 2.06e + 01	0.128
		model-2	2751	$u$ 8.68e + 00	0.027
Klein-Gordon Eq. 7	angle-Cascade	771	$u$ 1.17e + 01 $f$ 3.17e + 00	2.727	
	classical PINN	model-1	7851	$u$ 1.75e + 01 $f$ 3.35e + 00	0.718
		model-2	2751	$u$ 1.76e + 01 $f$ 3.78e + 00	0.358
Convection Diffusion Eq. 8	angle-Cascade	821	$u$ 1.20e + 01 $f$ 4.38e + 00	0.008	
	classical PINN	model-1	7901	$u$ 2.00e + 01 $f$ 3.11e + 00	0.014
		model-2	2801	$u$ 2.06e + 01 $f$ 1.31e + 01	0.1

equation 8. This expansion allows us to assess whether the advantages of our quantum-enhanced architecture persist across problems with fundamentally different physical characteristics and computational challenges.

Table 4 presents the performance of the angle-cascade DV-circuit QCPINN model for solving these three additional PDEs and comparing the results with the classical models. Our angle-cascade QCPINN model maintains its parameter efficiency advantage while achieving competitive or better accuracy compared to classical PINNs. For the wave equation, our model requires only a 9.8% parameters while achieving a 50.5% reduction in relative  $L_2$  error. The Klein-Gordon equation presents additional complexity due to its coupled system nature. Although our model exhibits a slightly higher final training loss, it maintains comparable relative  $L_2$  errors while using only 9.8% of the parameters required by model-1. Notably, for the convection-diffusion equation, our angle-cascade QCPINN with 821 parameters

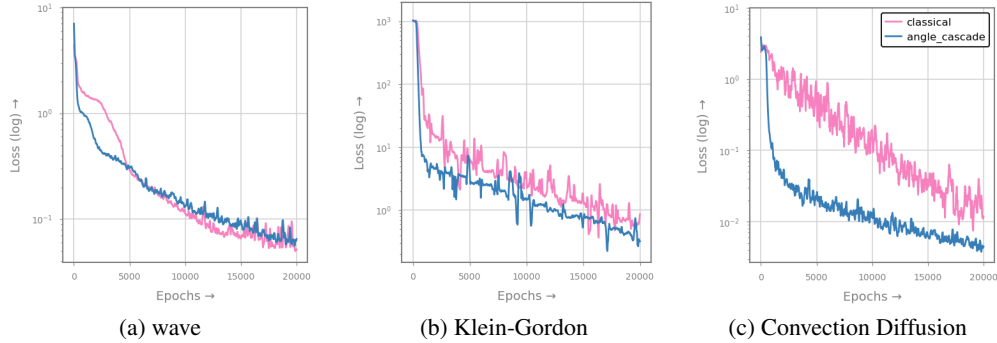


Figure 8: Training loss history for three PDEs: (a) wave, (b) Klein-Gordon, and (c) convection-diffusion. Each plot compares the convergence behavior of our angle-cascade (which outperforms the other embedding and topologies) QCPINN model against the best-performing classical PINN model (as reported in table 4) over 20,000 training epochs.

(compared to 7,901 in model-1) achieves a 43% reduction in relative  $L_2$  error for the primary solution variable and demonstrates improved training convergence.

Figure 8 compares the convergence behavior of the angle-cascade DV-circuit QCPINN model to the classical PINN model. For the wave equation, figure 8(a) shows that the angle-cascade QCPINN (blue line) demonstrates significantly faster initial convergence, achieving lower loss values within the first 5,000 epochs compared to the classical approach (pink line). Likewise, for the Klein-Gordon equation, figure 8(b) shows that angle-cascade QCPINN maintains comparable convergence stability despite the equation’s coupled nature, with both models exhibiting similar loss trajectories after the initial training phase. Notably, for the convection-diffusion equation, figure 8(c) shows that our model consistently maintains a monotonic loss reduction throughout training, reaching a final loss approximately one order of magnitude lower than that of the classical approach.

Figure 9 visualizes both exact and predicted solutions. For the wave equation, figure 9(a) shows that both the classical PINN and QCPINN capture the oscillatory pattern, but the error distribution of QCPINN (top-right plot) displays noticeably lower error magnitudes across the domain. The Klein-Gordon equation, figure 9(b), shows our model’s ability to accurately represent coupled solutions, with error distributions that are comparable to or better than those of the classical model. The convection-diffusion equation, figure 9(c), shows our model’s ability to precisely capture the sharp localized features characteristic of convection-dominated flows. The error visualization confirms significantly reduced prediction errors across solution components ( $u$  and  $f$ ), with error magnitudes approximately 2 – 3 times lower than those of classical PINNs.

## 7 Conclusion

We found that QCPINN models achieve comparable solution accuracy to classical PINNs while requiring a fraction of trainable parameters – as little as 10% of those needed by their classical counterparts under about the same settings. The experimental evidence supports our hypothesis that hybrid quantum-classical approaches can maintain solution quality while dramatically improving parameter efficiency. Our systematic exploration across multiple PDEs (including Helmholtz, Lid-driven Cavity Flow, Klein-Gordon, Wave, and convection-diffusion equations) consistently revealed that DV-circuit implementations with angle embedding and cascade circuit configurations offer superior performance. Most notably, for the convection-diffusion equation, our angle-cascade QCPINN achieved around 40% reduction in relative  $L_2$  error compared to classical models.

This study’s primary strength lies in its comprehensive comparative framework, systematically evaluating various quantum circuit architectures (DV and CV), embedding strategies (amplitude and angle), and DV circuit topologies (alternate, cascade, cross-mesh, and layered) across multiple PDE types. The open-source implementation further enhances reproducibility and enables community engagement. However, we acknowledge several limitations. While parameter efficiency was significantly improved, overall solution accuracy remained comparable to classical PINNs rather than surpassing them, except for the convection-diffusion problem. Additionally, the highly non-convex PINN loss landscapes still required careful weighting for the loss terms, which were determined through extensive empirical studies rather than exploring QC approaches to enhance this solution. Contrary to theoretical expectations, CV-circuit implementations exhibited training instabilities and underperformed relative to DV-circuit variants for the cases considered in this study.



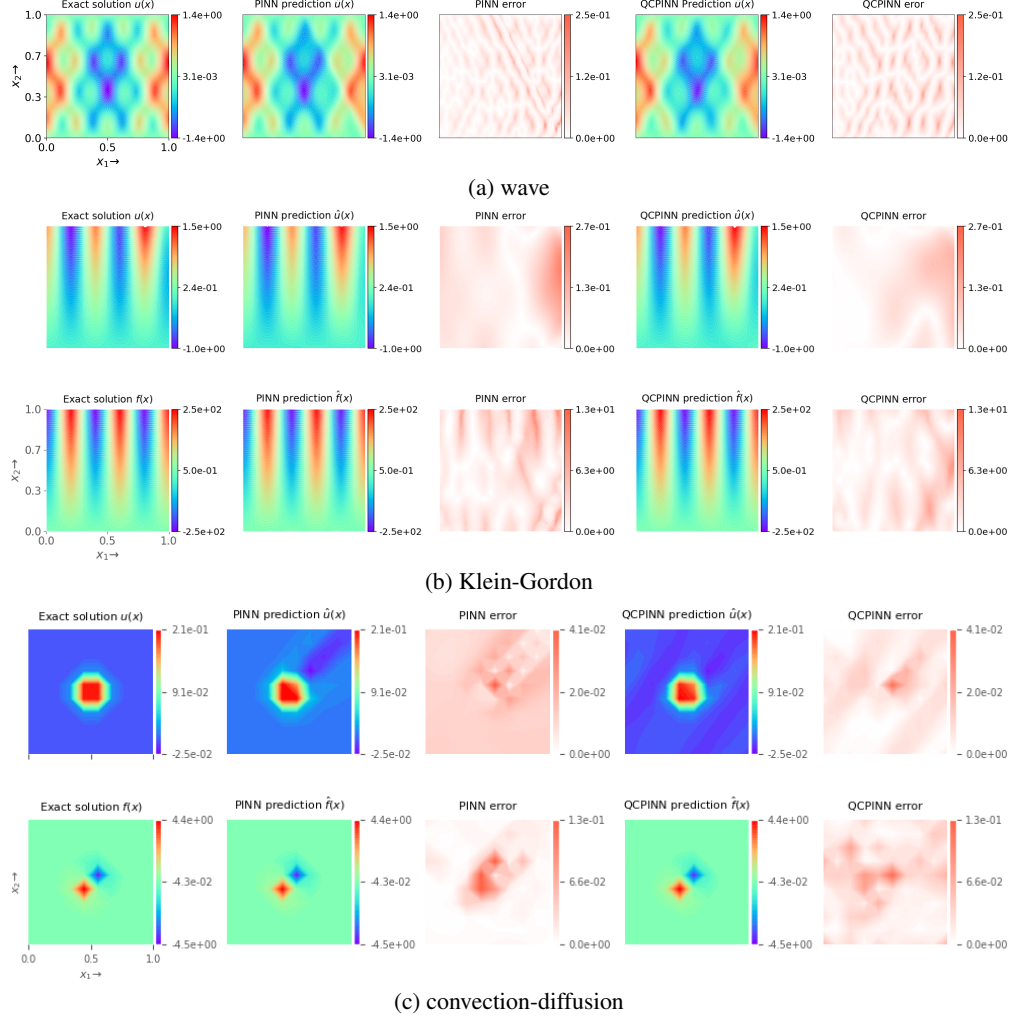


Figure 9: Comparison of the exact solution and the model predictions for three PDEs: (a) wave, (b) Klein-Gordon, and (c) convection-diffusion. For each equation, we present results from both the best-performing classical PINN model and our angle-cascade DV-circuit QCPINN implementation. The top row displays the velocity field ( $u$ ), while the bottom row shows the force field ( $f$ ).

Despite these limitations, our findings remain robust when examined through multiple performance metrics and across diverse PDE types. The consistent advantage of angle-cascade configurations in achieving lower relative  $L_2$  errors and final training losses, combined with their significant parameter efficiency, represents a meaningful advancement in physics-informed machine learning.

Future work could use more complex PDEs that necessitate significantly larger parameter spaces. By subsequently applying PINN and QPINN to these challenging scenarios, a comparative analysis could reveal more compelling evidence of QCPINN's benefits and potentially uncover additional advantages not observed in simpler problem domains or that PINN can not address. Through such an expanded investigation, the field may develop a more comprehensive understanding of when and how quantum-enhanced neural networks significantly outperform classical approaches for solving complex differential equations.

Future research should also focus on exploring advanced quantum circuit designs specifically optimized for PDE characteristics, investigating performance in larger-scale physical systems, and developing alternative optimization strategies to enhance training stability, especially for CV-circuit quantum methods. Additionally, the findings that quantum-enhanced methods performed particularly well on problems with multiple physical scales or sharp localized features require deeper investigation.

## Acknowledgment

We thank the National Center for High-Performance Computing of Turkiye (UHem) for providing computing resources under grant number 5010662021.

**Keywords** Quantum Computing · Neural networks · Physics-informed neural network · Partial differential equation · PINN · PDE

## References

- [1] Xue Ying. An overview of overfitting and its solutions. In *Journal of physics: Conference series*, volume 1168, page 022022. IOP Publishing, 2019.
- [2] Kosuke Mitarai, Makoto Negoro, Masahiro Kitagawa, and Keisuke Fujii. Quantum circuit learning. *Physical Review A*, 98(3):032309, 2018.
- [3] Vojtěch Havlíček, Antonio D Córcoles, Kristan Temme, Aram W Harrow, Abhinav Kandala, Jerry M Chow, and Jay M Gambetta. Supervised learning with quantum-enhanced feature spaces. *Nature*, 567(7747):209–212, 2019.
- [4] Marco Cerezo, Andrew Arrasmith, Ryan Babbush, Simon C Benjamin, Suguru Endo, Keisuke Fujii, Jarrod R McClean, Kosuke Mitarai, Xiao Yuan, Lukasz Cincio, et al. Variational quantum algorithms. *Nature Reviews Physics*, 3(9):625–644, 2021.
- [5] Maria Schuld, Ryan Sweke, and Johannes Jakob Meyer. Effect of data encoding on the expressive power of variational quantum-machine-learning models. *Physical Review A*, 103(3):032430, 2021.
- [6] Amira Abbas, David Sutter, Christa Zoufal, Aurélien Lucchi, Alessio Figalli, and Stefan Woerner. The power of quantum neural networks. *Nature Computational Science*, 1(6):403–409, 2021.
- [7] Yuxuan Du, Min-Hsiu Hsieh, Tongliang Liu, Shan You, and Dacheng Tao. Learnability of quantum neural networks. *PRX quantum*, 2(4):040337, 2021.
- [8] Alexandr Sedykh, Maninadh Podapaka, Asel Saginalieva, Karan Pinto, Markus Pflitsch, and Alexey Melnikov. Hybrid quantum physics-informed neural networks for simulating computational fluid dynamics in complex shapes. *Machine Learning: Science and Technology*, 5(2):025045, 2024.
- [9] Nahid Binandeh Dehaghani, A Pedro Aguiar, and Rafal Wisniewski. A hybrid quantum-classical physics-informed neural network architecture for solving quantum optimal control problems. In *2024 IEEE International Conference on Quantum Computing and Engineering (QCE)*, volume 1, pages 1378–1386. IEEE, 2024.
- [10] Corey Trahan, Mark Loveland, and Samuel Dent. Quantum physics-informed neural networks. *Entropy*, 26(8):649, 2024.
- [11] Fong Yew Leong, Wei-Bin Ewe, Tran Si Bui Quang, Zhongyuan Zhang, and Jun Yong Khoo. Hybrid quantum physics-informed neural network: Towards efficient learning of high-speed flows. *arXiv preprint arXiv:2503.02202*, 2025.
- [12] Maziar Raissi, Paris Perdikaris, and George E Karniadakis. Physics-informed neural networks: A deep learning framework for solving forward and inverse problems involving nonlinear partial differential equations. *Journal of Computational Physics*, 378:686–707, 2019.
- [13] Nathan Killoran, Thomas R Bromley, Juan Miguel Arrazola, Maria Schuld, Nicolás Quesada, and Seth Lloyd. Continuous-variable quantum neural networks. *Physical Review Research*, 1(3):033063, 2019.
- [14] Jarrod R McClean, Sergio Boixo, Vadim N Smelyanskiy, Ryan Babbush, and Hartmut Neven. Barren plateaus in quantum neural network training landscapes. *Nature communications*, 9(1):4812, 2018.
- [15] Marco Cerezo, Akira Sone, Tyler Volkoff, Lukasz Cincio, and Patrick J Coles. Cost function dependent barren plateaus in shallow parametrized quantum circuits. *Nature communications*, 12(1):1791, 2021.
- [16] Zoë Holmes, Kunal Sharma, Marco Cerezo, and Patrick J Coles. Connecting ansatz expressibility to gradient magnitudes and barren plateaus. *PRX quantum*, 3(1):010313, 2022.
- [17] Francesco Tacchino, Panagiotis Barkoutsos, Chiara Macchiavello, Ivano Tavernelli, Dario Gerace, and Daniele Bajoni. Quantum implementation of an artificial feed-forward neural network. *Quantum Science and Technology*, 5(4):044010, 2020.
- [18] Stefano Mangini, Francesco Tacchino, Dario Gerace, Daniele Bajoni, and Chiara Macchiavello. Quantum computing models for artificial neural networks. *Europhysics Letters*, 134(1):10002, 2021.



- [19] Aram W Harrow, Avinatan Hassidim, and Seth Lloyd. Quantum algorithm for linear systems of equations. *Physical review letters*, 103(15):150502, 2009.
- [20] Andris Ambainis. Variable time amplitude amplification and quantum algorithms for linear algebra problems. In *STACS'12 (29th Symposium on Theoretical Aspects of Computer Science)*, volume 14, pages 636–647. LIPIcs, 2012.
- [21] Rolando Somma, Andrew Childs, and Robin Kothari. Quantum linear systems algorithm with exponentially improved dependence on precision. In *APS March Meeting Abstracts*, volume 2016, pages H44–001, 2016.
- [22] Sarah K Leyton and Tobias J Osborne. A quantum algorithm to solve nonlinear differential equations. *arXiv preprint arXiv:0812.4423*, 2008.
- [23] Dominic W Berry. High-order quantum algorithm for solving linear differential equations. *Journal of Physics A: Mathematical and Theoretical*, 47(10):105301, 2014.
- [24] Andrew M Childs and Jin-Peng Liu. Quantum spectral methods for differential equations. *Communications in Mathematical Physics*, 375(2):1427–1457, 2020.
- [25] Dominic W Berry, Andrew M Childs, Aaron Ostrander, and Guoming Wang. Quantum algorithm for linear differential equations with exponentially improved dependence on precision. *Communications in Mathematical Physics*, 356:1057–1081, 2017.
- [26] Jeffrey Yepez. Quantum lattice-gas model for the burgers equation. *Journal of Statistical Physics*, 107:203–224, 2002.
- [27] Ashley Montanaro and Sam Pallister. Quantum algorithms and the finite element method. *Physical Review A*, 93(3):032324, 2016.
- [28] Furkan Oz, Rohit KSS Vuppala, Kursat Kara, and Frank Gaitan. Solving burgers’ equation with quantum computing. *Quantum Information Processing*, 21(1):30, 2022.
- [29] Furkan Oz, Omer San, and Kursat Kara. An efficient quantum partial differential equation solver with chebyshev points. *Scientific Reports*, 13(1):7767, 2023.
- [30] John Preskill. Reliable quantum computers. *Proceedings of the Royal Society of London. Series A: Mathematical, Physical and Engineering Sciences.*, 454(1969):385–410, 1998.
- [31] Barbara M Terhal. Quantum error correction for quantum memories. *Reviews of Modern Physics*, 87(2):307–346, 2015.
- [32] Andrew M Childs, Yuan Su, Minh C Tran, Nathan Wiebe, and Shuchen Zhu. Theory of trotter error with commutator scaling. *Physical Review X*, 11(1):011020, 2021.
- [33] Sergey Bravyi and Alexei Kitaev. Universal quantum computation with ideal clifford gates and noisy ancillas. *Physical Review A—Atomic, Molecular, and Optical Physics*, 71(2):022316, 2005.
- [34] Sergio Boixo, Sergei V Isakov, Vadim N Smelyanskiy, Ryan Babbush, Nan Ding, Zhang Jiang, Michael J Bremner, John M Martinis, and Hartmut Neven. Characterizing quantum supremacy in near-term devices. *Nature Physics*, 14(6):595–600, 2018.
- [35] Scott Aaronson. Read the fine print. *Nature Physics*, 11(4):291–293, 2015.
- [36] Carlo Ciliberto, Mark Herbster, Alessandro Davide Ialongo, Massimiliano Pontil, Andrea Rocchetto, Simone Severini, and Leonard Wossnig. Quantum machine learning: a classical perspective. *Proceedings of the Royal Society A: Mathematical, Physical and Engineering Sciences*, 474(2209):20170551, 2018.
- [37] Seth Lloyd, Masoud Mohseni, and Patrick Rebentrost. Quantum algorithms for supervised and unsupervised machine learning. *arXiv preprint arXiv:1307.0411*, 2013.
- [38] Maria Schuld and Nathan Killoran. Quantum machine learning in feature hilbert spaces. *Physical review letters*, 122(4):040504, 2019.
- [39] Seth Lloyd, Maria Schuld, Aroosa Ijaz, Josh Izaac, and Nathan Killoran. Quantum embeddings for machine learning. *arXiv preprint arXiv:2001.03622*, 2020.
- [40] Kerstin Beer, Dmytro Bondarenko, Terry Farrelly, Tobias J Osborne, Robert Salzmann, Daniel Scheiermann, and Ramona Wolf. Training deep quantum neural networks. *Nature communications*, 11(1):808, 2020.
- [41] Adrián Pérez-Salinas, David López-Núñez, Artur García-Sáez, P. Forn-Díaz, and José I. Latorre. One qubit as a universal approximant. *Physical Review A*, 104:012405, Jul 2021.
- [42] Takahiro Goto, Quoc Hoan Tran, and Kohei Nakajima. Universal approximation property of quantum machine learning models in quantum-enhanced feature spaces. *Physical Review Letters*, 127(9):090506, 2021.

- [43] Yunchao Liu, Srinivasan Arunachalam, and Kristan Temme. A rigorous and robust quantum speed-up in supervised machine learning. *Nature Physics*, 17(9):1013–1017, 2021.
- [44] Yudong Cao, Jonathan Romero, Jonathan P Olson, Matthias Degroote, Peter D Johnson, Mária Kieferová, Ian D Kivlichan, Tim Menke, Borja Peropadre, Nicolas PD Sawaya, et al. Quantum chemistry in the age of quantum computing. *Chemical reviews*, 119(19):10856–10915, 2019.
- [45] Bela Bauer, Sergey Bravyi, Mario Motta, and Garnet Kin-Lic Chan. Quantum algorithms for quantum chemistry and quantum materials science. *Chemical Reviews*, 120(22):12685–12717, 2020.
- [46] Benjamin Nachman, Davide Provasoli, Wibe A De Jong, and Christian W Bauer. Quantum algorithm for high energy physics simulations. *Physical review letters*, 126(6):062001, 2021.
- [47] Carlo A Trugenberger. Quantum pattern recognition. *Quantum Information Processing*, 1:471–493, 2002.
- [48] Alberto Peruzzo, Jarrod McClean, Peter Shadbolt, Man-Hong Yung, Xiao-Qi Zhou, Peter J Love, Alán Aspuru-Guzik, and Jeremy L O’Brien. A variational eigenvalue solver on a photonic quantum processor. *Nature communications*, 5(1):4213, 2014.
- [49] Jarrod R McClean, Jonathan Romero, Ryan Babbush, and Alán Aspuru-Guzik. The theory of variational hybrid quantum-classical algorithms. *New Journal of Physics*, 18(2):023023, 2016.
- [50] Carlos Bravo-Prieto, Ryan LaRose, Marco Cerezo, Yigit Subasi, Lukasz Cincio, and Patrick J Coles. Variational quantum linear solver. *Quantum*, 7:1188, 2023.
- [51] Anton Simen Albino, Lucas Correia Jardim, Diego Campos Knupp, Antonio Jose Silva Neto, Otto Menegasso Pires, and Erick Giovanni Sperandio Nascimento. Solving partial differential equations on near-term quantum computers. *arXiv preprint arXiv:2208.05805*, 2022.
- [52] Oleksandr Kyriienko, Annie E Paine, and Vincent E Elfving. Solving nonlinear differential equations with differentiable quantum circuits. *Physical Review A*, 103(5):052416, 2021.
- [53] Daniel Bultrini and Oriol Vendrell. Mixed quantum-classical dynamics for near term quantum computers. *Communications Physics*, 6(1):328, 2023.
- [54] Annie E Paine, Vincent E Elfving, and Oleksandr Kyriienko. Quantum kernel methods for solving regression problems and differential equations. *Physical Review A*, 107(3):032428, 2023.
- [55] Michael Lubasch, Jaewoo Joo, Pierre Moinier, Martin Kiffner, and Dieter Jaksch. Variational quantum algorithms for nonlinear problems. *Physical Review A*, 101(1):010301, 2020.
- [56] Samuel L Braunstein and Peter Van Loock. Quantum information with continuous variables. *Reviews of modern physics*, 77(2):513–577, 2005.
- [57] Stefano Markidis. On physics-informed neural networks for quantum computers. *Frontiers in Applied Mathematics and Statistics*, 8:1036711, 2022.
- [58] Abhishek Setty, Rasul Abdusalamov, and Felix Motzoi. Self-adaptive physics-informed quantum machine learning for solving differential equations. *Machine Learning: Science and Technology*, 6(1):015002, 2025.
- [59] John Preskill. Quantum computing in the nisq era and beyond. *Quantum*, 2:79, 2018.
- [60] Kishor Bharti, Alba Cervera-Lierta, Thi Ha Kyaw, Tobias Haug, Sumner Alperin-Lea, Abhinav Anand, Matthias Degroote, Hermann Heimonen, Jakob S Kottmann, Tim Menke, et al. Noisy intermediate-scale quantum algorithms. *Reviews of Modern Physics*, 94(1):015004, 2022.
- [61] Aditi Krishnapriyan, Amir Gholami, Shandian Zhe, Robert Kirby, and Michael W Mahoney. Characterizing possible failure modes in physics-informed neural networks. *Advances in neural information processing systems*, 34:26548–26560, 2021.
- [62] Sifan Wang, Shyam Sankaran, Hanwen Wang, Yue Yu, Andrew Paris, and Paris Perdikaris. Approximation analysis of physics-informed neural networks under the neural tangent kernel framework. *Neural Networks*, 153:123–140, 2022.
- [63] Yeonjong Shin, Zhongqiang Zhang, and George Em Karniadakis. Error estimates of residual minimization using neural networks for linear pdes. *Journal of Machine Learning for Modeling and Computing*, 4(4), 2023.
- [64] Afrah Fareaa and Mustafa Serdar Celebi. Learnable activation functions in physics-informed neural networks for solving partial differential equations, 2024.
- [65] Ville Bergholm, Josh Izaac, Maria Schuld, Christian Gogolin, Shah Nawaz Ahmed, Vishnu Ajith, M Sohaib Alam, Guillermo Alonso-Linaje, B Akash Narayanan, Ali Asadi, et al. PennyLane: Automatic differentiation of hybrid quantum-classical computations. *arXiv preprint arXiv:1811.04968*, 2018.

- [66] Michael Broughton, Guillaume Verdon, Trevor McCourt, Antonio J Martinez, Jae Hyeon Yoo, Sergei V Isakov, Philip Massey, Ramin Halavati, Murphy Yuezhen Niu, Alexander Zlokapa, et al. Tensorflow quantum: A software framework for quantum machine learning. *arXiv preprint arXiv:2003.02989*, 2020.
- [67] Zongyi Li, Nikola Kovachki, Kamyar Azizzadenesheli, Burigede Liu, Kaushik Bhattacharya, Andrew Stuart, and Anima Anandkumar. Fourier neural operator for parametric partial differential equations. *arXiv preprint arXiv:2010.08895*, 2020.
- [68] Edward Farhi and Hartmut Neven. Classification with quantum neural networks on near term processors. *arXiv preprint arXiv:1802.06002*, 2018.
- [69] Sukin Sim, Peter D Johnson, and Alán Aspuru-Guzik. Expressibility and entangling capability of parameterized quantum circuits for hybrid quantum-classical algorithms. *Advanced Quantum Technologies*, 2(12):1900070, 2019.
- [70] Ben Jaderberg, Abhishek Agarwal, Karsten Leonhardt, Martin Kiffner, and Dieter Jaksch. Minimum hardware requirements for hybrid quantum–classical dmft. *Quantum Science and Technology*, 5(3):034015, 2020.
- [71] Lukas Mouton, Florentin Reiter, Ying Chen, and Patrick Rebentrost. Deep-learning-based quantum algorithms for solving nonlinear partial differential equations. *Physical Review A*, 110(2):022612, 2024.
- [72] Nathan Killoran, Josh Izaac, Nicolás Quesada, Ville Bergholm, Matthew Amy, and Christian Weedbrook. Strawberry fields: A software platform for photonic quantum computing. *Quantum*, 3:129, 2019.
- [73] Alexander I Lvovsky. Squeezed light. *Photonics: Scientific Foundations, Technology and Applications*, 1:121–163, 2015.
- [74] A Ferraro, S Olivares, and MGA Paris. Gaussian states in quantum information (bibliopolis, napoli, 2005). *Dell’Anno et al., Phys. Rep.*, 428:53, 2006.
- [75] PD Drummond and DF Walls. Quantum theory of optical bistability. i. nonlinear polarisability model. *Journal of Physics A: Mathematical and General*, 13(2):725, 1980.
- [76] Josh Dees, Antoine Jacquier, and Sylvain Laizet. Unsupervised random quantum networks for pdes. *Quantum Information Processing*, 23(10):325, 2024.

## A CV-based QCPINN

---

### Algorithm 1 Continuous Variable Neural Network (CV-based QNN)

---

**Require:** Qumodes:  $num\_qumodes$ , Layers:  $num\_layers$ , Device:  $d$ , Cutoff:  $c$ , Input: Tensor  $x$

**Ensure:** Output: Tensor  $y$

```

1: Initialize Parameters:
2:  $\theta_1, \theta_2 \sim \mathcal{N}(0, 0.01\pi)$  (Interferometer),  $r_{disp}, r_{squeeze} \sim \mathcal{N}(0, 0.001)$  (Nonlinear)
3:  $kerr \sim \mathcal{N}(0, 0.001)$  (Kerr nonlinearity)
4: Quantum Device: Initialize  $d$  with  $num\_qumodes$ , cutoff  $c$ .
5: procedure QUANTUMCIRCUIT(input)
6:   for  $i = 1$  to  $num\_qumodes$  do
7:     Encode Inputs with Displacements  $D$ :  $D(\text{input}[i], 0)$  ▷ only real amplitudes
8:   end for
9:   for  $l = 1$  to  $num\_layers$  do
10:    Apply Interferometer( $\theta_1[l]$ )
11:    Apply Squeezing( $r_{squeeze}[l], 0.0$ )
12:    Apply Interferometer( $\theta_2[l]$ )
13:    Apply Displacement( $r_{disp}[l], 0.0$ )
14:    Apply Kerr( $kerr[l] \times 0.001$ )
15:   end for
16:   Measure state  $\langle \hat{q}_i \rangle$  for each wire.
17:   return Measurements
18: end procedure
19: procedure INTERFEROMETER( $\theta$ )
20:   for  $l = 1$  to  $num\_qumodes$  do
21:     for  $(q_1, q_2)$  in Pairs( $num\_qumodes$ ) do
22:       if  $(l + k) \% 2 \neq 1$  then
23:         Apply Beamsplitter  $B(\theta[n], 0.0)$ 
24:       end if
25:     end for
26:   end for
27:   for  $i = 1$  to  $num\_qumodes - 1$  do
28:     Apply Rotation  $R_Z(\theta[i])$ 
29:   end for
30: end procedure
31: procedure FORWARDPASS(Inputs  $x$ )
32:   Initialize an empty list for outputs
33:   for each  $s$  in  $x$  do
34:      $y \leftarrow$  QuantumCircuit( $s$ )
35:     Append  $y$  to outputs
36:   end for
37:   return outputs
38: end procedure

```

---

## B PDEs

### B.1 Helmholtz Equation

The Helmholtz equation represents a fundamental PDE in mathematical physics, arising as the time-independent form of the wave equation. We consider a two-dimensional Helmholtz equation of the form:

$$\begin{aligned} \Delta u(x, y) + k^2 u(x, y) &= f(x, y) & (x, y) \in \Omega \\ u(x, y) &= h(x, y) & (x, y) \in \Gamma_0 \end{aligned} \quad (4)$$

where  $\Delta$  is the Laplacian operator defined as  $\Delta u = \frac{\partial^2 u}{\partial x^2} + \frac{\partial^2 u}{\partial y^2}$ ,  $k$  is the wavenumber (related to the frequency of oscillation),  $f(x, y)$  is the forcing term (source function),  $h(x, y)$  specifies the Dirichlet boundary conditions. In this study, we choose an exact solution of the form:

$$u(x, y) = \sin(a_1\pi x) \sin(a_2\pi y)$$

on the square domain  $\Omega = [-1, 1] \times [-1, 1]$  with Wavenumber  $k = 1$ , first mode number  $a_1 = 1$ , and the second mode number  $a_2 = 4$ . This choice of solution leads to a corresponding source term:

$$f(x, y) = u(x, y)[k^2 - (a_1\pi)^2 - (a_2\pi)^2]$$

To solve this problem using QCPINN, we construct a loss function that incorporates both the physical governing equation and the boundary conditions:

$$\begin{aligned} \mathcal{L}(\theta) &= \min_{\theta} (\lambda_1 \|\mathcal{L}_{\text{phy}}(\theta)\|_{\Omega} + \lambda_2 \|\mathcal{L}_{\text{bc}}(\theta)\|_{\Gamma_0}) \\ &= \min_{\theta} (\lambda_1 \text{MSE}(\underbrace{\|u_{\theta_{xx}}(x, y) + u_{\theta_{yy}}(x, y) + \alpha u_{\theta}(x, y)\|_{\Omega}}_{\text{PDE residual}}) + \text{MSE}(\lambda_2 \underbrace{\|u_{\theta}(x, y) - u(x, y)\|_{\Gamma_0}}_{\text{Boundary condition}})) \end{aligned}$$

where  $\alpha = (a_1\pi)^2 + (a_2\pi)^2$  combines the mode numbers into a single parameter. The chosen loss weights are  $\lambda_1 = 1.0$  and  $\lambda_2 = 10.0$ .

## B.2 Time-dependent 2D lid-driven cavity Problem

The lid-driven cavity flow is a classical CFD benchmark problem that is a fundamental test case for many numerical methods where flow is governed by the unsteady, incompressible Navier-Stokes equations. The momentum equation, continuity equation, initial condition, no-slip boundary on walls, and moving lid condition are defined, respectively, as :

$$\begin{aligned} \rho \left( \frac{\partial \mathbf{u}}{\partial t} + \mathbf{u} \cdot \nabla \mathbf{u} \right) &= -\nabla p + \mu \nabla^2 \mathbf{u} \\ \nabla \cdot \mathbf{u} &= 0 \\ \mathbf{u}(0, \mathbf{x}) &= 0 \\ \mathbf{u}(t, \mathbf{x}_0) &= 0 \quad \mathbf{x} \in \Gamma_0 \\ \mathbf{u}(t, \mathbf{x}_l) &= 1 \quad \mathbf{x} \in \Gamma_1 \end{aligned} \tag{5}$$

The computational domain is  $\Omega = (0, 1) \times (0, 1)$ , the spatial discretization,  $(N_x, N_y) = (100, 100)$  is uniform grid, with temporal domain  $t \in [0, 10]$  seconds and  $\Delta t = 0.01s$  with density  $\rho = 1056 \text{ kg/m}^3$ , viscosity  $\mu = 1/\text{Re} = 0.01 \text{ kg/(m}\cdot\text{s)}$ , where Re is the Reynolds number.  $\Gamma_1$  is the top boundary (moving lid) with tangential velocity  $U = 1 \text{ m/s}$ , and  $\Gamma_0$  is the remaining three sides with no-slip condition ( $\mathbf{u} = 0$ ) where  $\mathbf{u} = (u, v)$ .

For validation purposes, we compare the neural network approximation with results obtained using the finite volume method. The PINN approach employs a composite loss function:

$$\mathcal{L}(\theta) = \min_{\theta} \left[ \lambda_1 \underbrace{\|\mathcal{L}_{\text{phy}}(\theta)\|_{\Omega}}_{\text{PDE residual}} + \lambda_2 \underbrace{\|\mathcal{L}_{\text{up}}(\theta) + \mathcal{L}_{\text{bc}_1}(\theta)\|_{\Gamma_1 \cup \Gamma_0}}_{\text{Boundary conditions}} + \lambda_3 \underbrace{\|\mathcal{L}_{\text{u0}}(\theta)\|_{\Omega}}_{\text{Initial conditions}} \right]$$

where, the physics-informed loss component,  $\mathcal{L}_{\text{phy}}(\theta)$  consists of three terms:

$$\mathcal{L}_{\text{phy}}(\theta) = \mathcal{L}_{r_u} + \mathcal{L}_{r_v} + \mathcal{L}_{r_c}$$

such that,

$$\begin{aligned} \mathcal{L}_{r_u}(\theta) &= \text{MSE} \left[ \left( u_{\theta_t} + u_{\theta} u_{\theta_x} + v_{\theta} u_{\theta_y} \right) + \frac{1.0}{\rho} p_{\theta_x} - \mu (u_{\theta_{xx}} + u_{\theta_{yy}}) \right] \\ \mathcal{L}_{r_v}(\theta) &= \text{MSE} \left[ \left( v_{\theta_t} + u_{\theta} v_{\theta_x} + v_{\theta} v_{\theta_y} \right) + \frac{1.0}{\rho} p_{\theta_y} - \mu (v_{\theta_{xx}} + v_{\theta_{yy}}) \right] \\ \mathcal{L}_{r_c}(\theta) &= \text{MSE} [u_{\theta_x} + v_{\theta_y}] \end{aligned}$$

The boundary and initial conditions are enforced through the following:

$$\begin{aligned}\mathcal{L}_{\text{up}} &= \text{MSE} [(1.0 - \hat{u}) + \hat{v}] \\ \mathcal{L}_{\text{bc1}} &= \mathcal{L}_{\text{bottom, right, left}} = \text{MSE} [\hat{u} + \hat{v}] \\ \mathcal{L}_{\text{u}_0} &= \text{MSE} [\hat{u} + \hat{v} + \hat{p}]\end{aligned}$$

where,  $\mathcal{L}_{\text{up}}$  is the moving lid,  $\mathcal{L}_{\text{bc1}}$  is the no-slip walls,  $\mathcal{L}_{\text{u}_0}$  is the initial conditions. The loss weights are empirically chosen as  $\lambda_1 = 0.1$ ,  $\lambda_2 = 2.0$ ,  $\lambda_3 = 4.0$  for  $\mathcal{L}_{\text{phy}}$ ,  $\mathcal{L}_{\text{up}}$ ,  $\mathcal{L}_{\text{bc1}}$  and  $\mathcal{L}_{\text{u}_0}$  respectively.

### B.3 1D Wave Equation

The wave equation is a fundamental second-order hyperbolic partial differential equation that models various physical phenomena. In its one-dimensional form, it describes the evolution of a disturbance along a single spatial dimension over time. The general form of the time-dependent 1D wave equation is:

$$\begin{aligned}u_{tt}(t, x) - c^2 u_{xx}(t, x) &= 0 & (t, x) \in \Omega \\ u(t, x_0) &= f_1(t, x) & (t, x) \text{ on } \Gamma_0 \\ u(t, x_1) &= f_2(t, x) & (t, x) \text{ on } \Gamma_1 \\ u(0, x) &= g(t, x) & (t, x) \in \Omega \\ u_t(0, x) &= h(t, x) & (t, x) \in \partial\Omega\end{aligned}\tag{6}$$

where  $u(t, x)$  represents the wave amplitude at position  $x$  and time  $t$ , and  $c$  is the wave speed characterizing the medium's properties. The subscripts denote partial derivatives:  $u_{tt}$  is the second time derivative, and  $u_{xx}$  is the second spatial derivative.

For our numerical investigation, we consider a specific case with the following parameters:  $c = 2$ ,  $a = 0.5$ ,  $f_1 = f_2 = 0$ . The exact solution is chosen as:

$$u(t, x) = \sin(\pi x) \cos(c\pi t) + 0.5 \sin(2c\pi x) \cos(4c\pi t)$$

This solution represents a superposition of two standing waves with different spatial and temporal frequencies. The problem is defined on the unit square domain  $(t, x) \in [0, 1] \times [0, 1]$ , leading to the specific boundary value problem:

$$\begin{aligned}u_{tt}(t, x) - 4u_{xx}(t, x) &= 0 & (t, x) \in \Omega = [0, 1] \times [0, 1] \\ u(t, 0) &= u(t, 1) = 0 \\ u(0, x) &= \sin(\pi x) + 0.5 \sin(4\pi x) & x \in [0, 1] \\ u_t(0, x) &= 0\end{aligned}$$

To solve this problem using the proposed hybrid CQPINN, we construct a loss function that incorporates the physical constraints, boundary conditions, and initial conditions:

$$\begin{aligned}\mathcal{L}(\theta) &= \min_{\theta} [\lambda_1 \|\mathcal{L}_{\text{phy}}(\theta)\|_{\Omega} + \lambda_2 \|\mathcal{L}_{\text{bc}}(\theta)\|_{\Gamma_1} + \lambda_3 \|\mathcal{L}_{\text{ic}}(\theta)\|_{\Gamma_0}] \\ &= \min_{\theta} [\lambda_1 \text{MSE}(\underbrace{\|u_{\theta_{tt}}(t, x) - 4u_{\theta_{xx}}(t, x)\|_{\Omega}}_{\text{PDE residual}}) \\ &\quad + \lambda_2 \text{MSE}(\underbrace{\|u_{\theta}(t, 0) + u_{\theta}(t, 1) + u_{\theta}(0, x) - \sin(\pi x) - 0.5 \sin(4\pi x)\|_{\Gamma_0 \cap \Gamma_1}}_{\text{Boundary/initial conditions}}) \\ &\quad + \lambda_3 \text{MSE}(\underbrace{\|u_{\theta_t}(0, x)\|_{\partial\Omega}}_{\text{Initial velocity}})]\end{aligned}$$

The loss weights are empirically chosen as  $\lambda_1 = 0.1$ ,  $\lambda_2 = 10.0$  and  $\lambda_3 = 0.1$ .

## B.4 Klein-Gordon Equation

The Klein-Gordon equation is a significant second-order hyperbolic PDE that emerges in numerous theoretical physics and applied mathematics areas. The equation represents a natural relativistic extension of the Schrödinger equation. In this study, we consider the one-dimensional nonlinear Klein-Gordon equation of the form:

$$\begin{aligned}
u_{tt} - \alpha u_{xx} + \beta u + \gamma u^k &= 0 & (t, x) \in \Omega \\
u(t, x) &= g_1(t, x) & (t, x) \text{ on } \Gamma_0 \\
u_t(t, x) &= g_2(t, x) & (t, x) \text{ on } \Gamma_1 \\
u(0, x) &= h(t, x) & (t, x) \in \partial\Omega \times [0, T]
\end{aligned} \tag{7}$$

where  $\alpha$  is the wave speed coefficient,  $\beta$  is the linear term coefficient,  $\gamma$  is the nonlinear term coefficient, and  $k$  is the nonlinearity power. For our numerical study, we set  $\alpha = 1$ ,  $\beta = 0$ ,  $\gamma = 1$  and  $k = 3$ . We choose an exact solution of the form:

$$u(t, x) = x \cos(5\pi t) + (tx)^3$$

This solution combines oscillatory behavior with polynomial growth, providing a challenging test case for our numerical method. The complete boundary value problem on the unit square domain becomes:

$$\begin{aligned}
u_{tt}(t, x) - u_{xx}(t, x) + u^3(t, x) &= 0 & (t, x) \in \Omega = [0, 1] \times [0, 1] \\
u(t, 0) &= 0 \\
u(t, 1) &= \cos(5\pi t) + t^3 \\
u(0, x) &= x \\
u_t(0, x) &= 0
\end{aligned}$$

To solve this nonlinear PDE using the proposed QCPINN, we construct a composite loss function incorporating the physical constraints, boundary conditions, and initial conditions:

$$\begin{aligned}
\mathcal{L}(\theta) &= \min_{\theta} [\lambda_1 \|\mathcal{L}_{\text{phy}}(\theta)\|_{\Omega} + \lambda_2 \|\mathcal{L}_{\text{bc}}(\theta)\|_{\Gamma_1} + \lambda_3 \|\mathcal{L}_{\text{ic}}(\theta)\|_{\Gamma_0}] \\
&= \min_{\theta} [\lambda_1 \text{MSE}(\| \underbrace{u_{\theta_{tt}}(t, x) - u_{\theta_{xx}}(t, x) + u^3(t, x)}_{\text{PDE residual}} \|)_{\Omega} \\
&\quad + \lambda_2 \text{MSE}(\| \underbrace{u(t, 0) + u(t, 1) - \cos(5\pi t) + t^3 + u(0, x) - x}_{\text{Boundary/initial conditions}} \|)_{\Gamma_1} \\
&\quad + \lambda_3 \text{MSE}(\| \underbrace{u_{\theta_t}(0, x)}_{\text{Initial velocity}} \|)_{\partial\Omega}]
\end{aligned}$$

The loss weights are chosen empirically to balance the different components as  $\lambda_1 = 1.0$ ,  $\lambda_2 = 10.0$ , and  $\lambda_3 = 1.0$ .

## B.5 Convection-diffusion Equation

The problem focuses on solving the 2D convection-diffusion equation, a partial differential equation that models the transport of a quantity under convection (bulk movement) and diffusion (spreading due to gradients). The specific form considered here includes a viscous 2D convection-diffusion equation of the form:

$$\begin{aligned}
u_t + c_1 u_x + c_2 u_y - D \Delta u(x, y) &= 0 & (t, x, y) \in \Omega \\
u(t, \mathbf{x}) &= g_0(t, \mathbf{x}) & (t, \mathbf{x}) \in \Gamma_0 \\
u(t, \mathbf{x}) &= g_1(t, \mathbf{x}) & (t, \mathbf{x}) \in \Gamma_1 \\
u(0, \mathbf{x}) &= h(0, \mathbf{x}) & \mathbf{x} \in \partial\Omega \times [0, T]
\end{aligned} \tag{8}$$

where  $c_1$  is the convection velocity in the  $x$  direction,  $c_2$  is the convection velocity in the  $y$  direction,  $D$  is the diffusion coefficient, and  $\Delta = \frac{\partial^2}{\partial x^2} + \frac{\partial^2}{\partial y^2}$  is the Laplacian operator. For our numerical investigation, we choose an exact solution describing a Gaussian pulse:

$$u(t, x, y) = \exp(-100((x - 0.5)^2 + (y - 0.5)^2)) \exp(-t)$$

The corresponding initial condition is:

$$h(0, x, y) = \exp(-100((x - 0.5)^2 + (y - 0.5)^2))$$

We choose  $c_1 = 1.0$ ,  $c_2 = 1.0$ , and  $D = 0.01$ . The complete initial-boundary value problem on the unit cube domain becomes:

$$\begin{aligned} u_t(t, x, y) + u_x(t, x, y) + u_y(t, x, y) - 0.01(u_{xx}(t, x, y) + u_{yy}(t, x, y)) &= 0 \\ u(t, x, y) &= g(t, x, y) \\ u(0, x, y) &= h(x, y) \end{aligned}$$

where  $(t, x, y) \in \Omega = [0, 1] \times [0, 1] \times [0, 1]$  To solve this problem using the proposed QCPINN model, we formulate a loss function that incorporates the physical governing equation, boundary conditions, and initial conditions:

$$\begin{aligned} \mathcal{L}(\theta) &= \min_{\theta} (\lambda_1 \|\mathcal{L}_{\text{phy}}(\theta)\|_{\Omega} + \lambda_2 \|\mathcal{L}_{\text{bc}}(\theta)\|_{\Gamma_1} + \lambda_3 \|\mathcal{L}_{\text{ic}}(\theta)\|_{\Gamma_0}) \\ &= \min_{\theta} \left[ \lambda_1 \min(\underbrace{\|u_{\theta_t}(t, x, y) + u_{\theta_x}(t, x, y) + u_{\theta_y}(t, x, y) - 0.01(u_{\theta_{xx}}(t, x, y) + u_{\theta_{yy}}(t, x, y))\|_{\Omega}}_{\text{PDE residual}})} \right. \\ &\quad \left. + \lambda_2 \min(\underbrace{\|u(t, x, y) - g_1(t, x, y)\|_{\Gamma_1}}_{\text{Boundary conditions}}) + \lambda_3 \min(\underbrace{\|u_{\theta}(0, x, y) - h(x, y)\|_{\Omega_0}}_{\text{Initial conditions}}) \right] \end{aligned}$$

The loss weights are chosen to balance the different components  $\lambda_1 = 1.0$ ,  $\lambda_2 = 10.0$ , and  $\lambda_3 = 10.0$ .